Image-Adaptive Deconvolution for Three-Dimensional Deep Biological Imaging

Jacques Boutet de Monvel,* Eric Scarfone,† Sophie Le Calvez,*‡ and Mats Ulfendahl*
*Center for Hearing and Communication Research, Karolinska Institutet, Stockholm, Sweden; †Institut National de la Santé et de la Recherche Médicale, Université de Montpellier, Montpellier, France; and ‡Biozentrum der Universität Basel, Basel, Switzerland

ABSTRACT Deconvolution algorithms are widely used in conventional fluorescence microscopy, but they remain difficult to apply to deep imaging systems such as confocal and two-photon microscopy, due to the practical difficulty of measuring the system's point spread function (PSF), especially in biological experiments. Since a separate PSF measurement performed under the design optical conditions of the microscope cannot reproduce the true experimental conditions prevailing in situ, the most natural approach to solve the problem is to extract the PSF from the images themselves. We investigate here the approach of cropping an approximate PSF directly from the images, by exploiting the presence of small structures within the samples under study. This approach turns out to be practical in many cases, allowing significantly better restorations than with a design PSF obtained by imaging fluorescent beads in gel. We demonstrate the advantages of this approach with a number of deconvolution experiments performed both on artificially blurred and noisy test images, and on real confocal images taken within an in vitro preparation of the mouse hearing organ.

INTRODUCTION

Biological applications of three-dimensional fluorescence microscopy are faced with two main imaging problems: the presence of often important levels of random noise, and the blurring due to the optical system's finite resolution. These two problems are all the more acute in applications of confocal and two-photon microscopy (Pawley, 1995), especially when imaging deep inside a thick biological sample. In such cases, the scattering of light and the variations of refractive index induced by the cells, tissue, and other structures surrounding the region of interest often induce a significant loss in intensity and various distortions in the optical response of the system (Hell et al., 1993; Kam et al., 1997, 2001; Boutet de Monvel et al., 2001).

Noise problems can be reduced by processing the images with efficient adaptive denoising algorithms, such as wavelet denoising (Donoho and Johnstone, 1994; Donoho et al., 1995). This technique requires no specific knowledge of the system's optical characteristics, and it has proven very effective in application to three-dimensional confocal images (Boutet de Monvel et al., 2001). Deblurring the images (deconvolution), on the other hand, requires the knowledge of the impulse response, or point spread function (PSF) of the system. This function can be measured by imaging structures of a size lower than or comparable to the system's resolution. A common procedure to do this consists of acquiring images of fluorescent beads of subresolution size, either deposited on a slide or immersed inside a gel (Hiraoka et al., 1990; Gibson and Lanni, 1991). Besides being time-consuming, this kind of measurement has an important drawback when applied to images taken inside a thick biological specimen, as it does not allow one to reproduce the typical imaging conditions of the experiments. Indeed, due to the variability of the samples, each new experiment is performed in effect with a different imaging system, and even for constant acquisition settings and at low levels of noise, the shape of the PSF will vary significantly from one sample to another (Kam et al., 2001; Boutet de Monvel et al., 2001).

The consequences of possible errors in the PSF when applying deconvolution algorithms have not been much investigated theoretically or experimentally. It is clear, however, that using a PSF closer to the truth can lead to very significant improvements in the restoration, both in terms of an increase in the effective resolution of the images, and in the avoidance of artifacts. Although it is possible in some cases to insert beads within the region of interest inside the sample (Boutet de Monvel et al., 2001), very often this approach is not practical, and it is therefore necessary to look for alternative ways of measuring the PSF.

In this article, we investigate the approach of extracting this quantity directly from the images. Rather than designing sophisticated processing techniques to achieve this, we will concentrate on a very simple and, when applicable, most practical approach, which consists of cropping the PSF from beadlike structures naturally occurring within the tissue. A similar approach is of common use in another context, the restoration of astronomical images, where real or artificial guide stars offer natural candidates for pointlike sources, allowing one to correct dynamically the degradations caused on the ground by turbulent air flow in the atmosphere (Hardy et al., 1977; Primmerman et al., 1991; Fugate et al., 1991). Although it is quite frequent to detect small dotlike structures within fluorescent biological samples, it has not been ascertained whether the same idea can be applied successfully in the context of three-dimensional biological micros-

Submitted January 17, 2003, and accepted for publication June 23, 2003.
Address reprint requests to Jacques H. R. Boutet de Monvel, M1:00 ENT, Karolinska Sjukhuset, Karolinska Institutet, Stockholm, Sweden 17176. Tel.: 46-85-177-3215; E-mail: j.boutet.de.monvel@cfh.ki.se.
© 2003 by the Biophysical Society
0006-3495/03/12/3991/11 $2.00

copy. Indeed, the cropped structures must be small enough, and at the same time well-enough isolated from the surrounding background, to provide a usable approximation of the system's PSF. Our main point is that the actual constraints imposed on the size and shape of the structures that can be used leave enough flexibility to make this approach effective and easy to apply. In particular these structures need not be truly pointlike for the deconvolution to be effective. They can actually be of a size comparable to the system's resolution (as defined by Rayleigh's criterion as the half-maximum width of the in situ PSF), or even slightly larger.

To demonstrate this point, we present the results of deconvolution experiments performed both with artificially degraded test images, and with confocal images acquired inside an in vitro preparation of the hearing organ in the mouse (Le Calvez and Ulfendahl, 2000). The first set of experiments makes clear the advantages of using a PSF cropped from the images over a standard bead measurement. Indeed, the outcome of deconvolution happens to be very sensitive to mismatches in the gross characteristics of the PSF, such as its size (corresponding to the system's resolution), and possible asymmetries such as a tilt with respect to the optical axis. Although one may achieve a high degree of accuracy when measuring the system's PSF under optimized conditions, this accuracy will be useless if the PSF obtained is overall ill-matched to the conditions of the experiments.

On the other hand, deconvolution is much less sensitive to inaccuracies in finer details of the PSF, such as the out-of-focus Airy patterns, which are typically filtered out when a smoothing is applied to the image. The following argument may help to make our point clearer. The image of some structure present in the sample corresponds to a blurring of the in situ PSF with the shape of that structure. As long as the structure is not significantly larger than the resolution, this smoothing results in a loss of the finest details of the PSF, but the gross characteristics are preserved. It is important to realize that this is true largely independently of the shape of the structure considered. We will present examples of PSFs extracted from structures of a size comparable to the resolution, which are clearly not beadlike in shape (not even convex), and which allow significant deconvolution results. This flexibility in the size and shape of the structures used is the main reason for the success of the cropping approach that we propose.

This success is further exemplified by our deconvolutions of confocal images of the inner ear. For the three examples considered, the image deconvolved with the extracted PSF was found to be better resolved and to contain fewer artifacts than the deconvolutions using standard bead measurements. We stress that these images represent typical experimental conditions and not special or biased situations. From our experience, it is possible to extract a PSF usable for deconvolution from >50% of our confocal images, a figure which should only increase if a strategy for searching dotlike structures in the samples is followed during the experiments.

METHODS

PSF terminology

Since we are considering several different kinds of point-spread functions, it will be useful to clarify the terms which we use to distinguish among them. The PSF needed for a proper deconvolution is, by definition, the PSF by which the images are blurred. In numerical experiments, where this PSF is known exactly, we call it the *exact PSF*. In biological experiments, this PSF depends on the specific refractive properties of the sample, and we therefore refer to it as the *in situ PSF*. In principle, this PSF will vary with the position of the focal point inside the sample, but we assume for simplicity that to a good approximation, each confocal image is blurred by a well-defined and shift-invariant in situ PSF (Boutet de Monvel et al., 2001). By an approximate PSF we understand any determination of the in situ PSF, be it obtained by means of a bead experiment, a theoretical model, or any other means. We shall refer to the approximate PSF obtained by performing a measurement in conditions close to the design optical conditions of the microscope (e.g., by imaging small beads on a coverslip or in gel), as the design PSF of the microscope. Contrary to the in situ PSF, the design PSF is reproducible and determined by the system's optical setup (characteristics of the lens, optical path inside the microscope, and acquisition settings). We investigate here an alternative way of obtaining an approximate PSF, by cropping it from the images of small structures already present in the sample. We will refer to such an approximation as an *extracted PSF*.

Generation of the test images

The test images used in our numerical experiments were of the type shown in Fig. 1. This image consists of a three-dimensional array of the form $I_n = O * p + n$, where $O * p$ denotes the convolution of a known original image O

FIGURE 1 Experiments simulating the PSF extraction. (*A*) Sections through a three-dimensional test image (128 × 128 × 32 pixels), taken as original. The central view is a focal *x,y* section through the image, whereas the side views are lateral *y,z* and *x,z* sections. The small white rectangles on the borders of the images indicate the position of the sections within the stack. (Each view is a maximum projection through the width of the corresponding rectangles.) Two structures found in the images are indicated by arrows and labeled N_1 and N_2. (*B*) Same sections through the degraded image obtained by blurring with a known PSF and addition of Poisson noise. (*C*) Same sections through the wavelet-denoised image. (*A′*) Slices through the original image, showing the locations of the inserted structures I_1, I_2, and I_3, and the two natural structures N_1 and N_2 inside the stack. (*C′*) Same slices taken through the wavelet-denoised image. (*D*) Projections through the PSFs extracted from the structures I_1, I_2, I_3, N_1, and N_2. To illustrate the cropping process, for each extracted PSF, we show the original structure (cropped from the original image), the structure cropped from the wavelet denoised image before background removal, and the final extracted PSF after background removal. At the bottom of the figure are projections of the other PSFs used in the experiments: the exact PSF, two design PSFs D_1 and D_2, and two theoretical PSFs Th_1 and Th_2 that differ in size: Th_1 has been rescaled so that its HMWs are equal to those of D_1, whereas the HMWs of Th_2 match those of the exact PSF. (*E*) Line-plots of the quality ratio Q_2 as function of the number of iterations, for deconvolutions of the wavelet-denoised image using the different PSFs. The curves are labeled according to the PSF used in the restoration. Note that the presence of noise prevents one from achieving a perfect reconstruction, even when using the exact PSF. (*Bottom*) The table regroups the maximum Q_2 values achieved for the different PSFs.

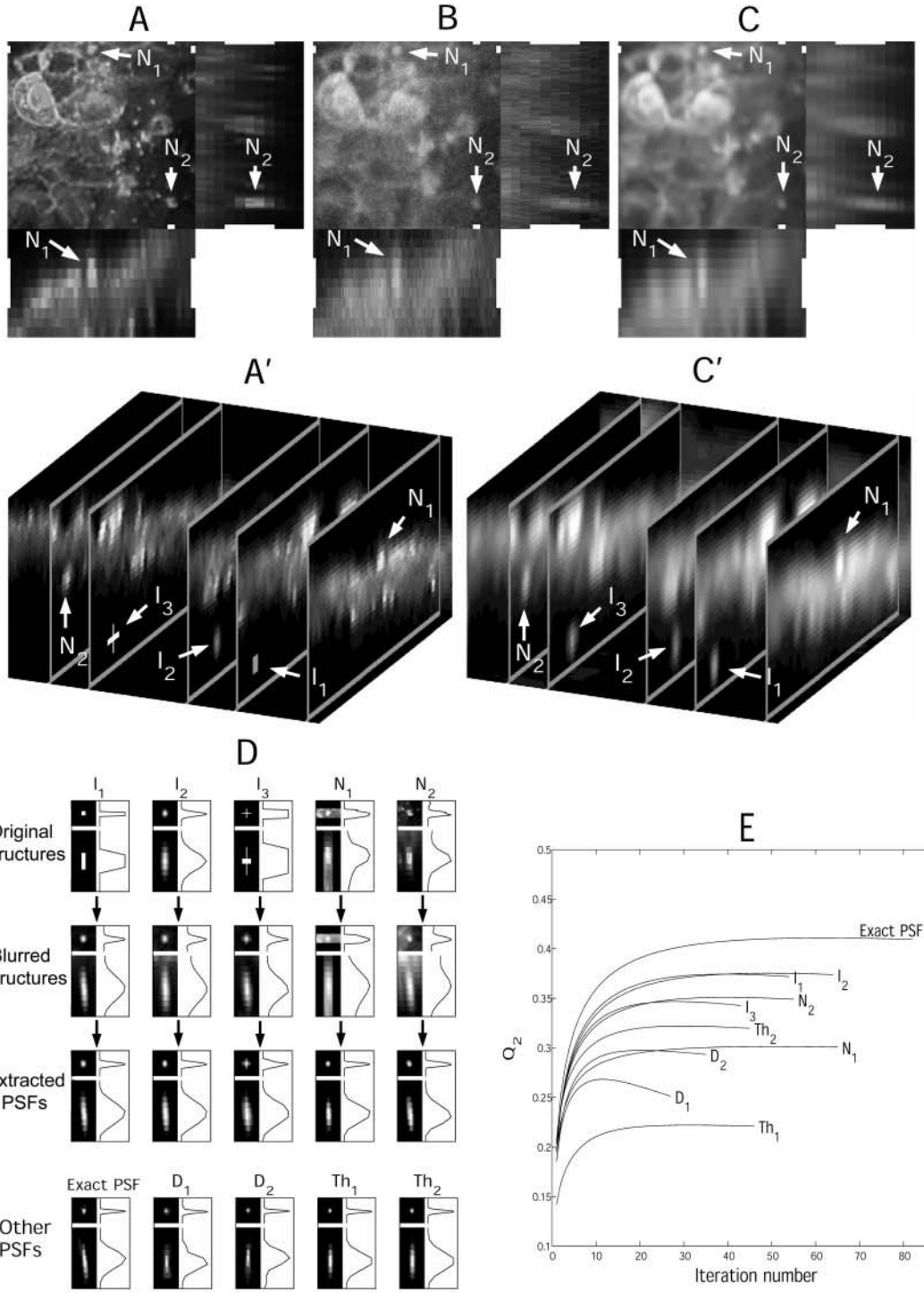

	I_1	I_2	I_3	N_1	N_2
$Q_2^{(max)}$ (%)	37.4	37.5	34.7	30.1	35.1

	Exact	D_1	D_2	Th_1	Th_2
$Q_2^{(max)}$ (%)	41.0	26.8	29.8	22.2	32.2

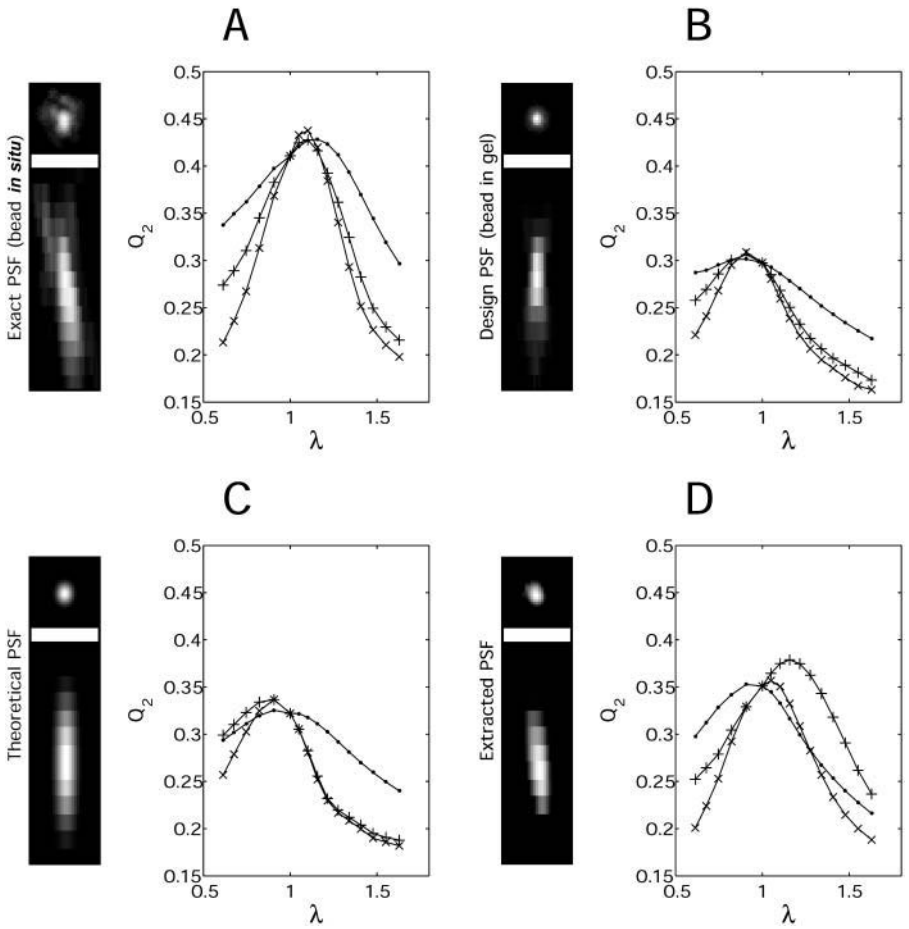

FIGURE 2 Effect of a mismatch in the size of the PSF. Each graph displays the results of restorations applied to the image of Fig. 1 *C*, for various rescalings of a reference PSF before deconvolution. We studied the behavior of the quality ratio Q_2 as a function of the factor λ by which the reference PSF was resized ($0.6 \leq \lambda \leq 1.6$). Results are plotted for three types of rescalings: along the three axes (x *symbols*), along the *z*-axis only (+ *symbols*), and along the *x*,*y*-axes only (● *symbols*). The graphs *A–D* correspond to different reference PSFs (see Fig. 1 *E*): (*A*) The exact PSF. (*B*) The design PSF D_1. (*C*) The theoretical PSF Th_2 (resized to the HMW of the exact PSF). (*D*) The extracted PSF N_2. Note the differences in the effects of rescalings along *x*,*y* and along *z*, a feature related to the asymmetry of confocal PSFs, which are typically 3–5× more extended along the optical axis than along the focal plane.

with a known PSF p, and n is a known random-noise component. The images O used as originals were obtained from real confocal images of the inner ear, previously processed by denoising and deconvolution. In the same way, the PSFs used for the blurring were actual confocal measurements acquired under various experimental conditions. To mimic the imaging process of a confocal microscope (Pawley, 1995), the noise component n was chosen to simulate Poisson statistics. In other words, the intensity $I_n(\mathbf{x})$ of each pixel $\mathbf{x} = (x,y,z)$ was taken at random independently, with a Poisson distribution of mean value $I_0(\mathbf{x}) = O * p(\mathbf{x})$.

Confocal microscopy

The images shown in Figs. 4–6 were acquired with a laser scanning confocal microscope (MRC1024, Bio-Rad, Hemel Hempstead, UK), using a water-immersion 40×/0.75 lens (Achroplan, Zeiss, Oberkochen, Germany), at several locations inside a temporal bone preparation of the mouse hearing organ (Le Calvez and Ulfendahl, 2000). The pixel formats and biological content of these images are indicated in the legends. For each acquisition, the pinhole radius, gain, and laser power of the microscope were adjusted so as to optimize the image contrast.

The fluorescent markers used in the preparation were calcein (Molecular Probes, Eugene, OR), which has an emission peak ~516 nm, and the dye RH795 (Molecular Probes), which emits ~630 nm. Both dyes were excited at 488 nm. For the one-channel images shown in Figs. 4 and 5, the RH795 emission only was detected using, for Fig. 4, a longpass filter (≥585 nm), and for Fig. 5, a bandpass filter (605 ± 16 nm). For the two-channel image shown in Fig. 6, RH795 was detected in the red channel, with a bandpass filter (605 ± 16 nm), whereas calcein was detected in the green channel, with a long-pass filter (≥522 nm).

Although the cross-talk should be minimal in the red channel with the filter configuration used, a certain amount of cross-talk is to be expected in the green channel (so that this channel contains presumably a proportion of both calcein and RH795 emissions). The main effect of this cross-talk, as far as deconvolution is concerned, will be to introduce a spatial variance in the PSF of the green channel, in regions where the two markers are not well co-localized. However, this variance is expected to be small, in any case much smaller than the distortions introduced by the sample (which are the same for both channels). Comparing the theoretical confocal PSFs predicted for the peak emission wavelengths of the two markers, one finds that although slightly different (with <6% difference in their half-maximum widths), these two PSFs can be considered identical for all practical purposes (they would produce nearly identical results when used in deconvolutions of our images). The possible distortions introduced by a cross-talk were therefore assumed to be an effect of smaller magnitude in our experiments, and these effects were not taken into account.

The PSFs used in our numerical experiments are shown in projection in Fig. 1 *E* and Fig. 2, *A–D*. The PSFs I_1, I_2, I_3, N_1, and N_2 from Fig. 1 *E* were extracted from the image shown in Fig. 1 *C* (see Results). The exact PSF used to blur the image and the PSFs D_1 and D_2 represent bead measurements acquired under similar acquisition settings. However, the PSFs D_1 and D_2 were obtained by imaging beads in agarose gel, whereas the exact PSF was measured by imaging beads placed inside a preparation of the guinea pig inner ear (Boutet de Monvel et al., 2001).

Step-by-step procedure for the PSF extraction

First step: denoising the images

A determination of the PSF obtained by cropping it directly from the raw image would have a poor signal-to-noise ratio and the resulting deconvolution would be unstable. Averaging is not very helpful here, as it is unlikely to find more than two or three suitable isolated structures within the same image. To deal with this problem, we applied the wavelet denoising technique to the images as described previously (Boutet de Monvel et al., 2001). The PSF extractions and deconvolutions were always performed on the denoised images.

Second step: searching for structures and cropping them

After the denoising, we searched the image by visual inspection for structures that could provide a suitable approximation to the in situ PSF. When small and isolated enough structures were found, a simple box cropping was applied to extract them, using a cropping box large enough that the structure would not be truncated. Often, additional structures were present within the cropping box, and had to be removed by hand. A simple masking was applied to do this: a small region was first selected around the structure of interest in the cropping box, taking care to avoid truncating this structure in regions where it produced an intensity above the background level. The pixels outside the selected region were then set to zero, leaving in the cropping box only the structure of interest.

Third step: removing the background

The extracted PSF was finally obtained by applying a soft thresholding (baseline subtraction) to the cropped structure, to remove the background, and to reduce possible truncation artifacts, which are another important source of instability in the deconvolution. The level to be subtracted was determined so that the extracted PSF would not show discontinuities within the cropping box. To do this we looked at the PSF intensity profiles along the x-, y-, z-axes, and we subtracted the highest level recorded near the boundaries of the profiles. In each case the resulting extracted PSF was checked visually, by verifying that its projections along the three axes did not show apparent discontinuities or truncation after the thresholding.

Deconvolution

Once a suitable determination of the PSF was obtained we applied a standard deconvolution algorithm to the wavelet denoised image as described previously (Boutet de Monvel et al., 2001). (For the two-channel image of Fig. 6, the PSF extractions and the deconvolutions were performed separately for each channel.) The deconvolution algorithm used was the Richardson-Lucy (RL) algorithm (Richardson, 1972, Lucy, 1974; Holmes, 1988), supplemented with a maximum-entropy regularization constraint (Gull and Daniell, 1978). Details on this algorithm are expanded in Boutet de Monvel et al. (2001). For the convenience of the reader, we rewrite here the iteration equation defining this algorithm,

$$f_{k+1}(\mathbf{x}) = f_k(\mathbf{x})\left(I/[f_k * p]\right) * \check{p}(\mathbf{x}) - T f_k(\mathbf{x}) \ln\left(f_k(\mathbf{x})\right), \quad (1)$$

where $f_k(\mathbf{x})$ is the deconvolved estimate after k iterations, $I(\mathbf{x})$ denotes the initial blurred image, $p(\mathbf{x})$ is the PSF normalized to unity ($\Sigma_{\mathbf{x}}\, p(\mathbf{x})=1$), $\check{p}(\mathbf{x})$ is defined by $\check{p}(\mathbf{x}) = p(-\mathbf{x})$, * denotes a convolution, and T is a parameter setting the strength of the maximum-entropy constraint. A padding was applied to the images before the deconvolution to minimize boundary artifacts. This consisted of adding a number of layers to the six faces of the original three-dimensional stack of images, using symmetry with respect to the original boundary layers to set the values of the added layers. The number of layers added on each face was determined in such a way that a PSF centered somewhere on the original boundary layers would not appear truncated in the padded image.

For the deconvolution of our test images, we used the RL algorithm (which amounts to using algorithm 1 with $T = 0$), applied to the wavelet-denoised images. The performance of the estimate $\hat{O}_k$ obtained after k RL iterations was quantified by its root-mean-squared error $\|\hat{O}_k - O\|_2 = (\Sigma_{\mathbf{x}} (\hat{O}_k(\mathbf{x}) - O(\mathbf{x}))^2)^{1/2}$. To get a normalized measure of this performance, we used a quality ratio defined by

$$Q_2 = 1 - \|\hat{O}_k - O\|_2 / \|I_n - O\|_2. \quad (2)$$

Perfect reconstruction occurs for $Q_2 = 1$, whereas a negative value of Q_2 indicates that something goes wrong with the restoration.

All the codes used for wavelet denoising, PSF extraction, and deconvolution were custom programs implemented in the Matlab language (The Mathworks, Natick, MA).

RESULTS AND DISCUSSION

Deconvolutions of artificially blurred test images

Simulating the PSF extraction

In the first experiment that we describe, we simulated the process of extracting the PSF on a test image, as illustrated in Fig. 1. Fig. 1, *A* and *B*, show sections of the original and of the degraded, blurred and noisy image, respectively (see Methods). Fig. 1 *C* shows the results of applying wavelet denoising to the degraded image. Fig. 1, A' and C', show the original and the denoised images under a different view consisting of a series of three-dimensional slices.

By searching the denoised image, two structures suitable for the PSF extraction were found, coming from structures already present in the original image. These two ''natural'' structures are the ones labeled N_1 and N_2 in the figures. In addition, we inserted three artificial structures in the original image before the degradation. These inserted structures (labeled I_1, I_2, and I_3) can be seen in Fig. 1, A' and C': I_1 is a rectangular spot of pixel size $5 \times 5 \times 3$. I_2 is a Gaussian spot having half-maximum widths (HMWs) of 6, 4.5, and 4 pixels along x, y, and z, respectively. I_3 is a crosslike spot made of three intersecting segments of diameters 5, 5, and 3 pixels along x, y, and z, respectively. The above sizes should be compared with the HMWs of the exact PSF used to blur the image, which were equal to 4, 3, and 4 pixels along x, y, and z, respectively.

For each of these structures, we applied the PSF extraction procedure described in Methods. The results are illustrated in Fig. 1 *D*, which displays projections of the original structures, the blurred structures cropped from the denoised image, and the extracted PSFs obtained after masking and background removal. We then used the extracted PSFs in a series of Richardson-Lucy (RL) deconvolutions applied to the denoised image. The results are summarized in the graph shown in Fig. 1 *E*, in which the values of the quality ratio Q_2 (compare to Eq. 2) is plotted as a function of the number of iterations, for the different PSFs used. In Fig. 1, the table at the bottom gives the maximum Q_2 value achieved in each case. For comparison, we included the results of deconvo-

lutions performed with five additional PSFs, shown in projection at the bottom of Fig. 1 *D*: the exact PSF, two designed PSFs D_1 and D_2 corresponding to standard bead measurements, and two ideal confocal PSFs Th_1 and Th_2 computed using a theoretical model. These last two PSFs were rescaled so that the HMWs of Th_1 and Th_2 matched the HMWs of D_1 and the exact PSF, respectively.

Note that none of the structures used in our PSF extractions can be considered as pointlike compared to the exact PSF. Moreover, these structures have rather arbitrary shapes (the cross and the structures N_1 and N_2 being not even assimilable to convex bodies.) It is clear, however, that once they have been blurred with the exact PSF, all of these structures look much more similar, and provide a better approximation to the exact PSF than, e.g., D_1 or D_2. Using the extracted PSFs for the deconvolution leads in fact to quality ratios comparable to the quality ratio achieved using the exact PSF. Additional experiments showed that the quality ratio obtained with the exact PSF was reproduced without significant change using a PSF extracted from a Gaussian or a rectangular spot of only half the sizes of I_1 and I_2.

The most stringent test of our extraction procedure, as well as the one which appears closest to the real experimental conditions, is provided by the results obtained with the structures N_1 and N_2. These structures are clearly not pointlike and are embedded in a significant background. The PSF extracted from N_2 allowed a deconvolution of a comparable quality as achieved with the PSFs extracted from the inserted structures I_1–I_3. The PSF extracted from N_1 was imbedded in a strong background (reaching 65% of its maximum value), and the corresponding quality ratio is smaller, but still >30%.

The deconvolutions using the nonextracted PSFs D_1, D_2, and Th_1 are of comparatively poorer quality, which we attribute to the obvious mismatches that these PSFs have in size and orientation with respect to the exact PSF. Note, however, that the theoretical PSF Th_2, which has been rescaled so that it has the same HMWs as the exact PSF, leads to a better deconvolution, of a quality ratio comparable to those achieved with the extracted PSFs. We shall come back to this observation below.

Influence of a mismatch in the size of the PSF

In a second set of experiments, we investigated the degradations occurring in the restoration when a mismatch is introduced between the PSF used in the deconvolution and the exact PSF. Although various kinds of mismatches may be considered, we limit ourselves to the degradation caused by changing the size of the PSF, because this effect appeared to be the most significant in our experiments. This effect is also natural to study, since the loss of resolution that results when focusing light inside a thick sample can be modeled by an increase in the PSF size.

The graphs shown in Fig. 2, *A*–*D*, summarize the results of four series of restorations applied to the same test image as in the previous experiment (Fig. 1). For each series, a given reference PSF $p_{\mathrm{ref}}(x,y,z)$ was rescaled by various amounts, producing a set of PSFs having the same shape, but different sizes. Each rescaled PSF was then used in a deconvolution applied to the wavelet-denoised image. The rescalings were of the form $p_{\mathrm{ref}}(x,y,z) \rightarrow p_{\mathbf{s}}(x,y,z) = C_{\mathbf{s}}\, p_{\mathrm{ref}}(x/s_x,\, y/s_y,\, z/s_z)$, where $\mathbf{s} = (s_x,s_y,s_z)$ is a vector of scaling parameters, and $C_{\mathbf{s}}$ a normalization constant chosen so that $\Sigma_{\mathbf{x}}\, p_{\mathbf{s}}(\mathbf{x}) = 1$. Cases *A*, *B*, *C*, and *D* correspond to different reference PSFs: the exact PSF, the design PSF D_1, the theoretical model Th_2, and the extracted PSF N_2, respectively (see Fig. 1 *D*). Each graph shows line plots of the quality ratio Q_2 of the best RL iteration (the iteration for which Q_2 was maximum) as a function of a scaling parameter λ, for three types of rescaling: 1), isotropic rescaling, $s_x = s_y = s_z = \lambda$; 2), rescaling along the *z*-axis, $s_x = s_y = 1$, $s_z = \lambda$; and 3), rescaling along the (x,y)-plane, $s_x = s_y = \lambda$, $s_z = 1$. In each case λ was made to vary between 0.6 and 1.6.

It is apparent from Fig. 2 *A* that a small mismatch in the size of the PSF has a significant effect on the quality of the restoration. This is reflected by a pronounced maximum of Q_2 as a function of λ for a value $\lambda \approx 1$. Note that the highest Q_2 value is obtained for a value of λ slightly larger than 1. This may appear surprising, since this means that a slight enlargement of the exact PSF induced a slight improvement in the deconvolution. Remember, however, that the deconvolutions were applied on the wavelet-denoised image. In effect, this amounts to applying a slight additional blurring to the image before the deconvolution. This blurring is not present in the exact PSF, since that PSF was not submitted to denoising. In fact, the maximum of Q_2 becomes sharper and closer to $\lambda = 1$ when the level of noise is lowered. The maximum becomes less pronounced and more displaced when errors are introduced in the PSF, as can be seen in the other graphs (Fig. 2, *B*–*D*). The relevance of the above observations for our purposes is clear. A PSF measured under optimized experimental conditions will have an uncontrolled mismatch in size and shape, which will induce significant degradations in the deconvolution. Such a mismatch will have a much better chance to be minimized with a PSF extracted from the image.

From another point of view, these experiments suggest that even when using an inaccurate PSF, a significant improvement may be achieved in the restoration by a suitable rescaling of the PSF. In this respect, the highest quality ratio, among the three approximate PSFs considered, was achieved using the extracted PSF. Although deconvolutions using the PSF D_1 had significantly lower quality ratios, a good deconvolution could still be achieved with an optimally rescaled theoretical model. This points to a possible generalization of our PSF extraction approach when dotlike structures are not easily found in the sample. Indeed, if the PSF cannot be obtained by simple cropping, it might still be possible to use information extracted from the image to infer correctly the parameters of a model. Note that an ideal

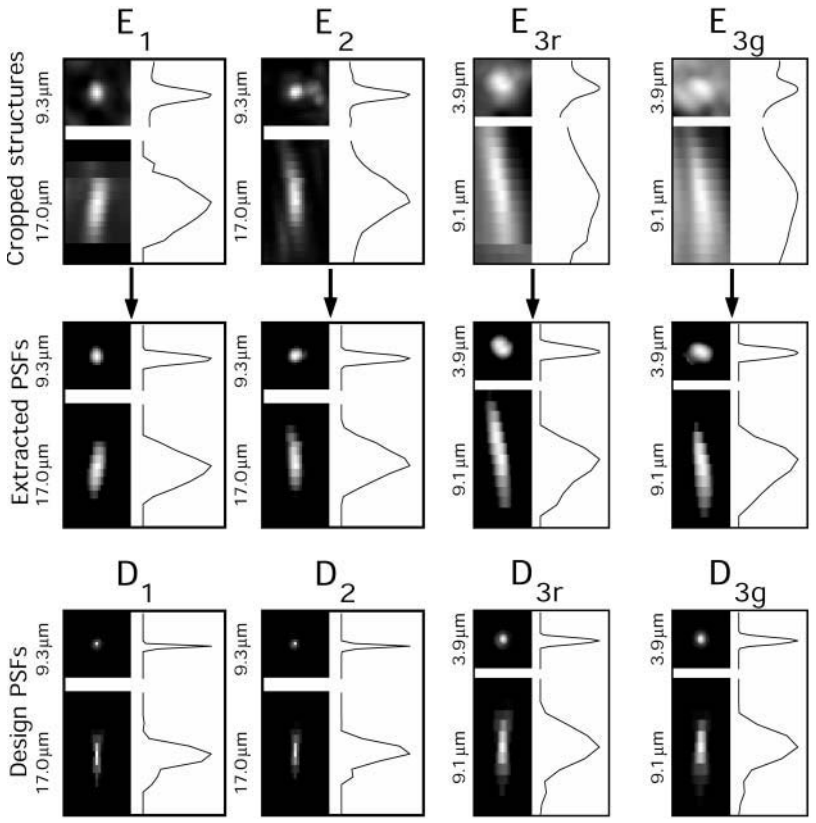

FIGURE 3 (*Top and middle*) Projections of the PSFs extracted from the confocal images shown in Figs. 4–6. The extracted PSFs are shown before and after the background removal. The labels E_1, E_2, and E_3 refer to the structures found in the corresponding denoised images (Figs. 4 *B*, 5 *B*, and 6 *B*, respectively). Although the same structure was used for both channels in Fig. 6, the extraction was performed separately on each channel, producing two distinct PSFs E_{3r} and E_{3g} for the red and green channel, respectively. (*Lower*) The corresponding design PSFs, obtained by imaging fluorescent beads in agarose gel. Note the differences in size and shape between the extracted and the design PSFs. The ratios of the half-maximum widths (HMWs) of E_1 to those of D_1 are ~1.6 along z, and 3 along x and y. The ratios between the HMWs of E_{3r} and D_{3r} are ~1.2 along z, and 2 along x and y.

confocal PSF, deduced solely from the excitation and emission wavelengths and the characteristics of the objective lens, would have a HMW along z typically ~5× smaller than the in situ PSF (which corresponds to $\lambda \approx 0.2$ in Fig. 2 *C*). In effect, this PSF would be too small to produce any significant improvement by deconvolution. Although we do not pursue this issue further here, it would clearly be of interest to dispose of reliable methods for fitting the parameters of a PSF model to a given image.

Deconvolutions of confocal images of the hearing organ

Two practical concerns one may have about the image restoration method we propose are, 1), whether small structures that are well enough isolated from the background occur often in the images; and 2), when the suitable structures are found, whether the truncation and background removal involved in cropping the PSF will not affect the deconvolution too much. Although the answer to the first point obviously depends on the samples under study, it is clear that dotlike structures are abundant in biological samples at the cellular level. Such structures are indeed easy to find in confocal images of the intact inner ear labeled with suitable fluorescent markers. To answer the second point, we applied deconvolutions to the confocal images shown in Figs. 4–6, using, on one side, PSFs extracted from these images, and on the other side, the corresponding design PSFs obtained by standard bead measurements under the same acquisition settings of the microscope. These PSFs are shown in projection in Fig. 3 which, together with Figs. 4–6, will serve to illustrate the process of PSF extraction and the subsequent deconvolutions.

PSF extraction

In each example, a small dotlike structure was found by visual inspection in the wavelet denoised image, and the PSF extraction procedure described in Methods was applied. In some images (for example in the image of Fig. 4), more than one suitable structure could be found. In each case we chose the structure that appeared best isolated from the surrounding background. The structures used in the first two images, labeled E_1, and E_2, are shown on Figs. 4 *B* and 5 *B*, respectively, together with the cropping boxes used in the extractions. From the image shown in Fig. 6, two different PSFs were extracted, one for each channel, corresponding to the images of one single structure through the two channels (labeled $E_{3r,g}$ on Fig. 6 *B*). These two PSFs are very similar, which is not surprising since the optical paths are the same for both channels and the differences induced by the different emission spectra of the two markers are expected to be small compared to the distortions introduced by the sample (compare to Methods).

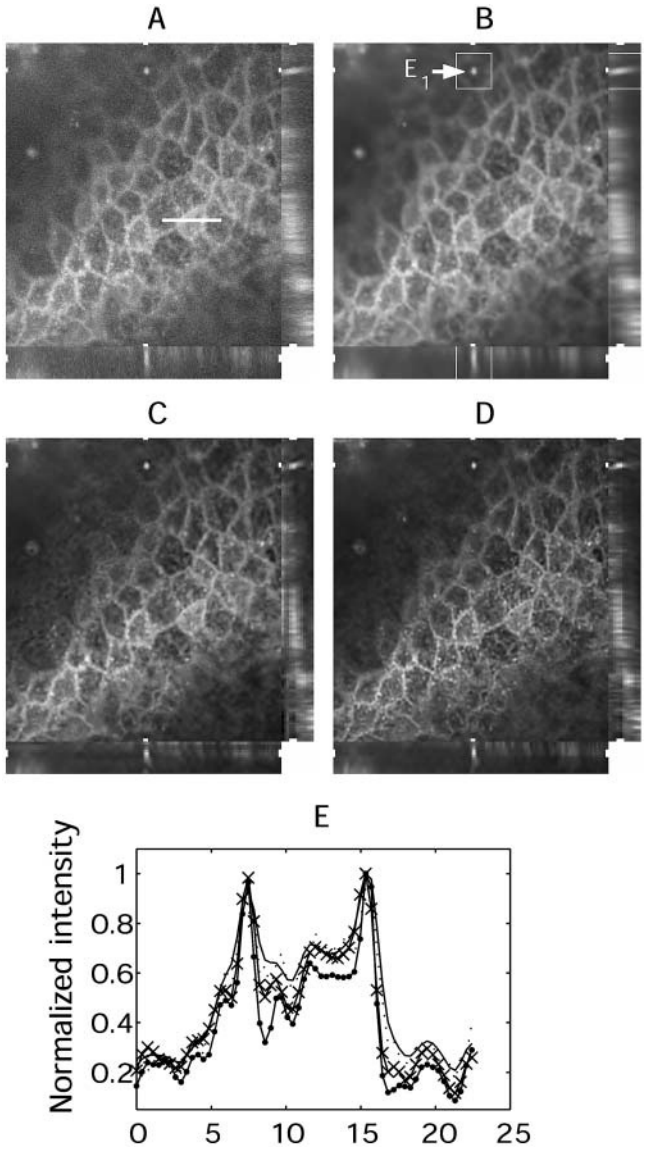

FIGURE 4 (*A*) Sections through a three-dimensional stack of confocal images (310 × 281 × 12, pixel size 0.374 μm × 0.374 μm × 1 μm) showing the Reissner's membrane above the auditory sensory hair cells of the hearing organ. (*B*) The same sections through the wavelet denoised image. The structure E_1 used for the PSF extraction is seen inside its cropping box and highlighted by the arrow. (*C*) Deconvolution using the design PSF shown in Fig. 3 D_1. (*D*) Deconvolution using the extracted PSF (Fig. 3 E_1). Both deconvolutions consisted of 100 iterations of Eq. 1 applied to the denoised image, with the maximum-entropy parameter T set to 0.007. (*E*) Line plots of the intensity profiles of the images along the scalebar (22.8 μm) shown in *A* (*A*, *dashed line*; *B*, *solid line*; *C*, x *symbols;* and *D*, ● *symbols*). For a better comparison the profiles have been divided by their respective maximum values.

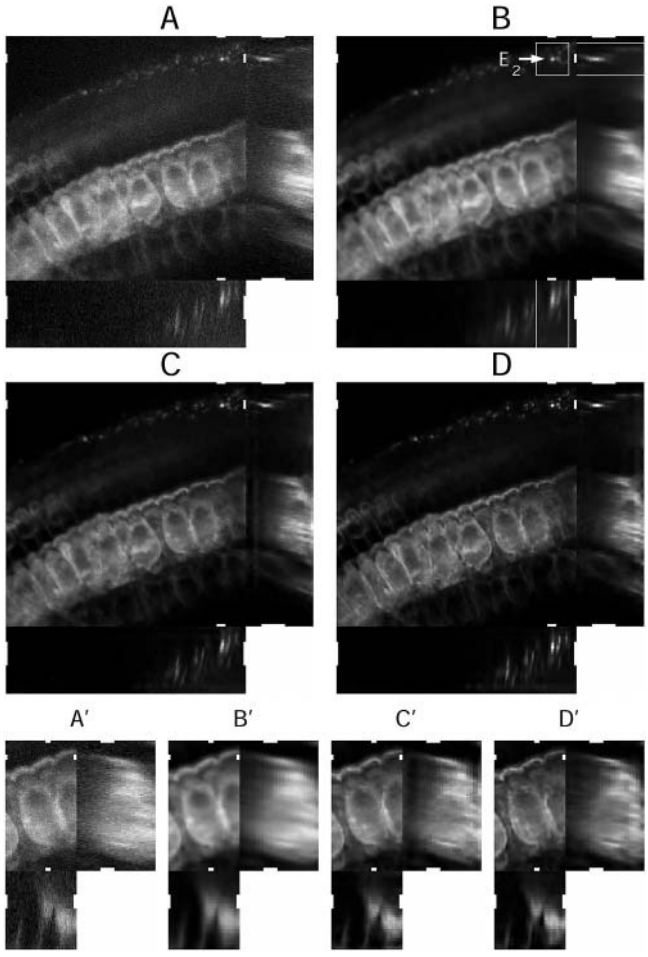

FIGURE 5 (*A*) Sections of a three-dimensional stack of confocal images (512 × 512 × 31, pixel size 0.374 μm × 0.374 μm × 1 μm), showing auditory sensory inner hair cells within the mouse hearing organ. (*B*) The same sections through the wavelet denoised image, showing the cropping box enclosing the structure E_2 used for the PSF extraction. (*C*) Deconvolution using the design PSF (Fig. 3 D_2). (*D*) Deconvolution using the extracted PSF (Fig. 3 E_2). Both deconvolutions consisted of 80 iterations of Eq. 1 applied to the denoised image, with the maximum-entropy parameter T set to 0.01. (*A′–D′*) Detail views of the same images, showing sections through a small region around one of the sensory hair cells.

Our extracted PSFs can only represent filtered and thresholded approximations of the true in situ PSFs. The structures used for cropping these PSFs are presumably slightly larger than the system's resolution, as smaller structures emit a signal too low to be well-distinguished from the background. The design PSFs represent more precise measurements, as far as the imaging characteristics of the system under optimized conditions are concerned. Typical Airy patterns are visible in these measurements, whereas such patterns are not resolved in the extracted PSFs. Our claim is that, nevertheless, the extracted PSFs are better matched to the images than are the design PSFs, for the purpose of image restoration. It is evident from Fig. 3 that the extracted PSFs have significantly larger extensions in space than the design PSFs. In addition, the design PSFs show no appreciable tilt with respect to the optical axis, whereas most extracted PSFs were tilted. We infer from these observations that the design PSFs presented mismatches in size and

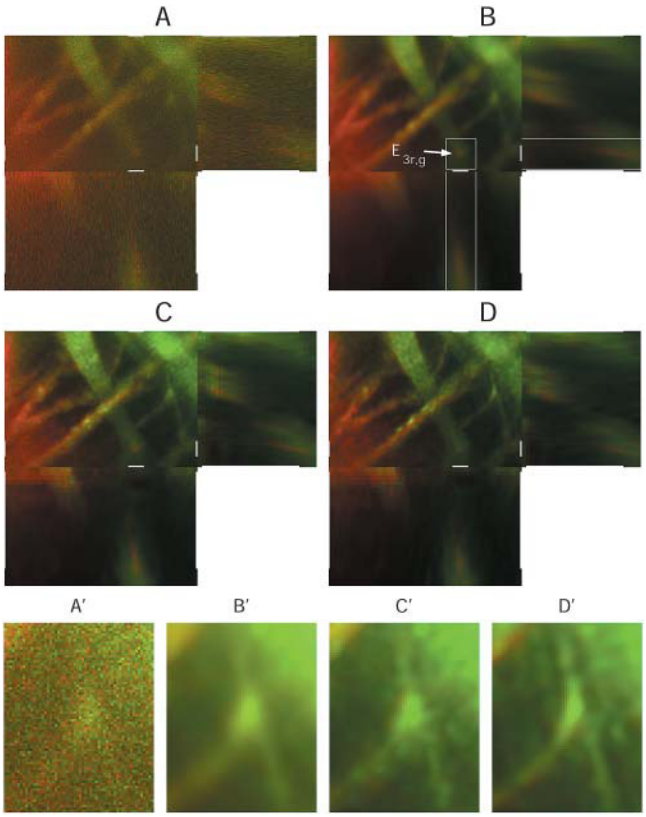

FIGURE 6 (*A*) Sections through a two-channel confocal image (181 × 256 × 28, pixel size 0.119 μm × 0.119 μm × 0.5 μm), showing nerve fibers crossing the tunnel of Corti inside the inner ear. The maximum projection along the optical axis has been extended to also show the structure that was used in the PSF extractions. (*B*) The same sections through the wavelet-denoised image, showing the cropping box enclosing the structure E_3 used for the PSF extraction. (*C*) Deconvolution using, for the red and green channels, the corresponding design PSFs (Fig. 3, D_{3r} and D_{3g}, respectively). (*D*) Deconvolution using, for the red and green channels, the corresponding extracted PSFs (Fig. 3, E_{3r} and E_{3g}, respectively). For each deconvolution, 80 iterations of Eq. 1 were applied to the denoised images, setting the maximum-entropy parameter T to 0.005 for the red channel and to 0.008 for the green channel. (*A′–D′*) Detail views of the same images, taken from a region of low contrast in the raw image, showing the process of two branching nerve fibers. Note the significantly better clarity achieved in the image deconvolved with the extracted PSF.

orientation with respect to the in situ PSF. These mismatches are very difficult, if not impossible to predict, and as we have seen in our experiments with test images, they induce significantly worse effects on deconvolution than a smoothing or a soft thresholding of the images.

Results of the deconvolutions

Comparing the deconvolution results obtained with the extracted PSFs to those obtained with the design PSFs provides good support to the above remarks. In each case, we found that using the extracted PSF led to a restoration of significantly higher quality than using the microscope's design PSF. To make this affirmation more precise, we shall rely both on quantitative criteria and visual impression. Fig. 4 *A* shows a confocal image of the Reissner's membrane lying above the auditory sensory hair cells of the hearing organ. Fig. 4, *B–D*, corresponds to the denoised image, the image deconvolved with the design PSF, and the image deconvolved with the extracted PSF, respectively. We stress that apart from using different PSFs in the deconvolution, in Fig. 4, *C* and *D* were processed and displayed in exactly the same way. In Fig. 4 *E*, we plotted normalized intensity profiles of these four images along the white line shown in Fig. 4 *A*.

The increase in effective resolution is visible from *C* to *D*, and is made clearly apparent on the profiles. If we assume that variations caused by artifacts are not significant in *C* and *D*, we can quantify this increase in resolution by comparing the frequency bandwidths (FBW) of the corresponding profiles. Using a common mean-square measure σ_k defined empirically for a given profile $f(x)$ by the formula $\sigma_k^2 = \int k^2|F(k)|^2\,dk / \int |F(k)|^2\,dk$ (where $F(k)$ denotes the Fourier transform of $f(x)$), we found that the FBW of *D* along the given line is ~1.4× that of *C*, 2.1× that of *B*, and 1.35× that of *A*. (The increase factor from *A* to *D* is smaller due to the fact that the raw image contains a significant amount of noise, and its FBW appears thereby artificially high.) In addition to this increase in resolution, one can note the presence of boundary artifacts in *C* along the optical axis, which are much less significant in *D*.

Fig. 5 shows a confocal view of a row of auditory sensory inner hair cells inside the mouse hearing organ. (Again, *A–D* correspond to the raw image, the denoised image, the deconvolution using the design PSF, and the deconvolution using the extracted PSF.) The increase in resolution from *C* to *D* is less dramatic than in the previous case, but it is still well visible, and corresponds to an increase in FBW of 9% for the displayed *x*,*y* sections. (The increase from *B* to *D* was, in this case, 55%). When looking into details of the image, it appears also that *C* contains significantly more artifacts than *D*, which results in a locally smoother image texture and a better contrast in *D*. This is apparent in the detail views *A′–D′*, where zoomed sections through one of the hair cells are displayed. One can notice in particular the better definition of the cell body and of the hair bundles in *D′*. It also becomes possible to make out details of the subcellular organization of the cells in a way not possible in the other images.

Fig. 6 is a two-channel confocal image showing nerve fibers crossing the tunnel of Corti inside the inner ear. In this case, the effective resolutions of the two deconvolved images (*C* and *D*) are not significantly different. (Although slightly higher, the FBW of *D* computed through the displayed *x*,*y* projection, differs from that of *C* by <1% for both channels.) However, the contrast of *C* is lowered by artifacts that are much less present in *D*. Again this is more apparent in the detail views *A′–D′* of the figure, showing the process of two

branching nerve fibers in a region of low contrast of the image.

CONCLUDING REMARKS

The above numerical tests, together with the experiments that we performed on confocal images of the mouse inner ear, clearly support the claims made in the Introduction. PSF measurements performed under the microscope's design conditions may be accurate for these conditions, but they are likely to be ill-matched to the actual conditions of the experiments when the images are acquired deep inside a thick and complex sample. Our experiments show that in such cases, a significant gain is achieved in the restoration by extracting the PSF directly from the images, which can be done if structures that are small and isolated enough are present in the sample. In other words, the same method that has proven so useful to astronomers can be fruitfully applied in the context of three-dimensional biological microscopy. When applicable, this method does not only allow one to save a significant amount of work, but it also makes deconvolution much easier to apply. Indeed, by definition, it does not require any particular knowledge of the acquisition settings of the images. Moreover, no specific constraint is imposed on the imaging system, apart from linearity and a reasonable shift-invariance. The method can be readily applied in particular to two-photon and wide-field fluorescence microscopies.

Clearly the direct cropping method used here has limitations. It cannot be applied as such when small dotlike structures are not visible inside the specimen. Although it is very frequent that suitable structures are present in the sample, the degree of accuracy achieved in an approximate PSF obtained by direct cropping remains limited, and under deep imaging conditions one should not expect to be able to make out the airy patterns of the in situ PSF using this method.

We point out that there is room for many extensions of the approach, which should make it all the more flexible in the future. More sophisticated adaptive processing methods (such as multiscale feature extractors and neural networks; Saito and Coifman, 1995) could be used to extract the PSF in a more effective and automatized way. Other structures than pointlike sources may also be used to estimate the PSF. For example, within the auditory system, the numerous nerve fibers projecting to the organ of Corti are good approximations of linelike structures. A section through such a structure could provide valuable information to construct a model PSF. More generally, a model-fitting approach to PSF extraction could be developed.

Other approaches to adaptive deconvolution have been proposed. In astronomy, adaptive optics tools based on deformable mirrors have been developed to trace the shape of a guide star in real-time (Primmerman et al., 1991; Fugate et al., 1991; Ragazzoni et al., 2000). PSF engineering techniques have been developed recently allowing investigators to partly adapt such tools to three-dimensional microscopy (Hanley et al., 1999; Neil et al., 2000). Ray tracing techniques provide another interesting approach to PSF estimation inside a thick biological sample (Kam et al., 2001). The main virtue of the approach proposed here, besides being very natural, is to be readily applicable (to our knowledge, for the first time) in many situations encountered in three-dimensional deep biological imaging without the need for specific optical devices or special care from the part of the experimentalist. This method is only a first step toward a fully adaptive deconvolution allowing one to treat dynamic situations where, strictly speaking, one is dealing with a different imaging system at each point of space and time. Although challenging, such adaptivity is nevertheless a goal that one will have to reach for a precise quantitation of live biological imaging.

We are grateful to Anders Fridberger for helpful discussions.

This work was supported by grants from the Swedish Research Council (09888), the Swedish Council for Work Life Research (1999-0512), the Foundation Tysta Skolan, the Swedish Institute, the Knut and Alice Wallenberg Foundation, the Petrus and Augusta Hedlund Foundation, and Institut National de la Santé et de la Recherche Médicale. J.B.d.M. acknowledges support from the European Community (Marie Curie fellowship) during the time of this work.

REFERENCES

Boutet de Monvel, J., S. Le Calvez, and M. Ulfendahl. 2001. Image restoration for confocal microscopy: improving the limits of deconvolution, with application to the visualization of the mammalian hearing organ. *Biophys. J.* 80:2455–2470.

Donoho, D. L., and I. M. Johnstone. 1994. Ideal spatial adaptation via wavelet shrinkage. *Biometrika.* 81:425–455.

Donoho, D. L., I. M. Johnstone, and M. Iain. 1995. Adapting to unknown smoothness via wavelet shrinkage. *J. Am. Stat. Assoc.* 90:1200–1224.

Fugate, R. Q., D. L. Fried, G. A. Ameer, B. R. Boeke, S. L. Browne, P. H. Roberts, R. E. Ruane, G. A. Tyler, and L. M. Wopat. 1991. Measurement of atmospheric wavefront distortion using a scattered light from a laser guide-star. *Nature.* 353:144–146.

Gibson, S. F., and F. Lanni. 1991. Experimental test of an analytical model of aberration in an oil-immersion objective lens used in three-dimensional light microscopy. *J. Opt. Soc. Am. A.* 8:1601–1613.

Gull, S. F., and G. J. Daniell. 1978. Image reconstruction from incomplete and noisy data. *Nature.* 272:686–690.

Hanley, Q. S., P. J. Verveer, M. J. Gemkow, D. Arndt-Jovin, and T. M. Jovin. 1999. An optical sectioning programmable array microscope implemented with a digital micromirror device. *J. Microsc.* 196:317–331.

Hardy, J. W., J. E. Lefebvre, and C. L. Koliopoulos. 1977. Using beacon stars to correct turbulence aberrations. *J. Opt. Soc. Am.* 67:360–369.

Hell, S., G. Reiner, C. Cremer, and E. H. K. Stelzer. 1993. Aberrations in confocal fluorescence microscopy induced by mismatches in refractive index. *J. Microsc.* 169:391–405.

Hiraoka, Y., J. W. Sedat, and D. A. Agard. 1990. Determination of the three-dimensional imaging properties of a light microscope system. *Biophys. J.* 57:325–333.

Holmes, T. J. 1988. Maximum likelihood image restoration adapted for noncoherent optical imaging. *J. Opt. Soc. Am. A.* 5:666–673.

Kam, Z., D. A. Agard, and J. W. Sedat. 1997. Three-dimensional microscopy in thick biological samples: a fresh approach for adjusting focus and correcting spherical aberration. *Bioimaging*. 5:40–49.

Kam, Z., B. Hanser, G. L. Gustafsson, D. A. Agard, and J. W. Sedat. 2001. Computational adaptive optics for live three-dimensional biological imaging. *Proc. Natl. Acad. Sci. USA*. 98:3790–3795.

Le Calvez, S., and M. Ulfendahl. 2000. An *in vitro* preparation to access cellular and neuronal components in the mouse inner ear. *J. Neurocytol.* 29:645–653.

Lucy, L. B. 1974. An iterative technique for the rectification of observed distributions. *Astron. J.* 79:745–754.

Neil, M. A. A., T. Wilson, and R. Juskaitis. 2000. Wavefront generator for complex pupil function synthesis and point spread function engineering. *J. Microsc.* 197:219–223.

Pawley, J. B. 1995. Handbook of Biological Confocal Microscopy. Plenum Press, New York.

Primmerman, C., D. V. Murphy, D. A. Page, and B. G. Zollars. 1991. Compensation of atmospheric optical distortion using a synthetic beacon. *Nature*. 353:141–143.

Ragazzoni, R., E. Marchetti, and G. Valente. 2000. Adaptive-optics corrections available for the whole sky. *Nature*. 403:54–56.

Richardson, W. H. 1972. Bayesian-based iterative method of image restoration. *J. Opt. Soc. Am.* 62:55–59.

Saito, N., and R. R. Coifman. 1995. Local discriminant bases and their applications. *J. Math. Imag. Vision*. 5:337–358.